IEEE Access
Multidisciplinary | Rapid Review | Open Access Journal

Received March 18, 2022, accepted April 2, 2022, date of publication April 6, 2022, date of current version April 13, 2022.

Digital Object Identifier 10.1109/ACCESS.2022.3165307

Electronic Nonlinearity of Full-Bridge PWM Inverter for Zero-Power PEMS System

LEI CHEN[1,2], JINMEI GUO[1], BIN ZHU[1], AND ZEYI ZHANG[3]
[1]School of Mechanical and Electronic Engineering, Jiangxi College of Applied Technology, Ganzhou 341000, China
[2]Longsheng Intelligent Equipment Company Ltd., Dongguan 523799, China
[3]School of Electrical Engineering and Automation, Jiangxi University of Science and Technology, Ganzhou 341000, China

Corresponding author: Zeyi Zhang (zhangzy@jxust.edu.cn)

This work was supported in part by the Science and Technology Research Project of Educational Department in Jiangxi Province under Grant GJJ210804, and in part by the High-Level Talents Research Start-Up Project of the Jiangxi University of Science and Technology under Grant 205200100476.

ABSTRACT The permanent-electro magnetic suspension (PEMS) technology takes advantage of the attractive magnetic force between the magnet and the iron core and reduces the power consumption eventually to zero. However, the active current in the electromagnet of the zero-power PEMS system fluctuates around zero due to external disturbances and suffers from the electronic nonlinearity of the driving circuit, such as the full-bridge pulse-width-modulation (PWM) inverter. This work presents that the 2 μs turn-off delay (*one electronic defect*) of the integrated circuit L298N (*one commercial full-bridge PWM inverter produced by STMicroelectronics*) leads to the nonlinear current-duty cycle characteristic, which undermines the control stability and limits the PWM frequency of the zero-power PEMS system. Moreover, the nonlinear mechanism is experimentally and theoretically analyzed for the critical PWM frequency and the sensitivity transition with respect to the 2 μs turn-off delay. Besides, the critical PWM frequency is of great significance for the energy efficiency and the dynamic performance of the high-speed PEMS transportation system.

INDEX TERMS Electromagnetics, DC-DC power converters, nonlinear network analysis, zero-power maglev.

I. INTRODUCTION

The electromagnetic suspension (EMS) technology has played an essential role in the maglev transportation industry in Germany, Japan, and China since 1960s [1]. Besides, the active magnetic bearing [2]–[4] is another successful application of the EMS technology and is widely found in flywheel systems, high-speed drives, and turbomolecular pumps. However, the EMS technology consumes considerably large power to generate sufficient attractive force against the gravity [5] and requires high-performance electronics, such as the isolated gate bipolar transistor (IGBT) [6]–[8] and the LLC resonant converter [5], [9].

In 1980s, the Nd-Fe-B permanent magnet was invented as a special functional material with huge magnetic energy accumulation. Since then, the permanent-electro magnetic suspension (PEMS) technology [5], [7], [10], [11] is economically effective by using the Nd-Fe-B permanent magnet to produce the attractive force and reduce the power consumption eventually to zero [10], [12], whereas the electromagnet only plays a dynamic regulatory role [6]. Mizuno *et al.* [13] developed an active vibration isolation system with an infinite stiffness against disturbances based on the zero-power PEMS technology. Zhang *et al.* [14] numerically optimized the geometry for the zero-power PEMS system as undergraduate project kits in terms of the zero-power force and the controller-gain requirement. Yalcin and Erkan [10] proposed linear-matrix-inequality (LMI) structures based on H_∞ and H_2 control approaches for 3-DoF micro vibration isolation with zero-power problem.

Due to its outstanding energy-saving and robust features, the zero-power PEMS technology also attracted great attention from the maglev transportation industry. Tzeng and Wang [15] presented a rigorous dynamic analysis for the high-speed maglev transportation system with the robust zero-power PEMS strategy. Zhang *et al.* [6] focused on the optimal structural design of the PEMS magnet and proposed optimized parameters with better carrying capability

The associate editor coordinating the review of this manuscript and approving it for publication was Gerardo Di Martino.

and lower suspension power loss. Cho *et al.* [16] reported a successful quadruple PEMS system with the improved zero-power control algorithm.

Importantly, unlike the non-zero-mean current (I) in the EMS technology [17], [18], the current for the zero-power PEMS technology fluctuates about zero due to external disturbances [8], [16]. Though the full-bridge pulse-width-modulation (PWM) inverter [2] (also known as the power converter [19] or the chopper [5]) can drive the zero-mean current in the electromagnet by the PWM duty cycle (D), there are few works analyzing its electronic nonlinearity that could be of great significance for the zero-power PEMS technology.

Moreover, the PWM frequency (f_{PWM}) is crucial for the dynamic performance of the high-speed PEMS transportation system, e.g., the disturbance rejection and the gap tracking [20]. In the literature, f_{PWM} is usually set from 10 kHz to 20 kHz [5], [8], [11], [17], [18]. Generally, in order to enhance the dynamic performance of the high-speed PEMS transportation system, higher f_{PWM} is under huge demand but may amplify the energy loss as well as the electronic nonlinearity of the full-bridge PWM inverter, which is to be discussed in the present work.

This work aims to analyze the electronic nonlinearity of the full-bridge PWM inverter for the zero-power PEMS system. The L298N full-bridge PWM inverter is chosen as the research target due to its wide application in low-power electronics, whereas the IGBT [6], [8] is mainly used for high-power usage. The paper starts with the mathematical model and the nonlinearity of the $I-D$ characteristic of the L298N full-bridge PWM inverter. Then, the nonlinear mechanism of the $I-D$ characteristic is further analyzed experimentally and theoretically, especially for the critical PWM frequency (f_{cr}) and the sensitivity transition with respect to (w.r.t.) the 2 μs turn-off delay. Nevertheless, concluding remarks are addressed.

II. CURRENT-DUTY CYCLE CHARACTERISTIC

A. MATHEMATICAL MODEL

Fig. 1 shows the electric circuit of the L298N full-bridge PWM inverter produced by STMicroelectronics. The inverter converts the PWM signal into the current in the electromagnet that is modelled as a serial combination of an inductance (L) and a resistance (R). $In1$ and $In2$ are two TTL logic-level input ports and control the voltages at Nodes M and N, denoted as U_M and U_N, respectively. For example, $U_M \approx +U$ when $In1$ = HIGH, and $U_M \approx 0\ V$ when $In1$ = LOW. Denote the current in the electromagnet as i_{MN} and the voltage across as $u_{MN} = U_M - U_N$. Hence, the relationship between i_{MN} and u_{MN} can be expressed as,

$$u_{MN} = Ri_{MN} + Ldi_{MN}/dt, \tag{1}$$

where u_{MN} is driven by the full-bridge PWM inverter and i_{MN} varies continuously due to the inductance. Relating physical properties are summarized in Table 1.

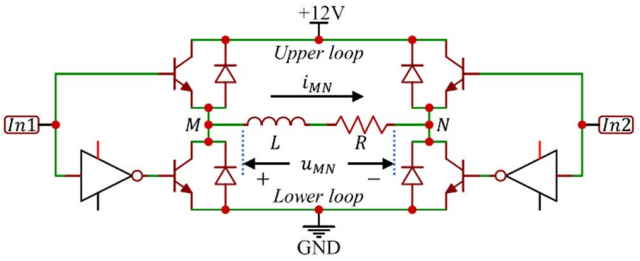

FIGURE 1. Electric circuit of L298N full-bridge PWM inverter.

TABLE 1. Physical properties.

Symbol	Quantity	Value	Unit
R	Electromagnet resistance	14.5	Ω
L	Electromagnet inductance	23.5	mH
τ	Electromagnet time constant	1.62	ms
U	Power supply voltage	12	V
f_{PWM}	PWM frequency	0.1-100	kHz
T	PWM period	0.01-10	ms

Moreover, Table 2 lists out three modes of the full-bridge PWM inverter with the electromagnet. When $In1 \neq In2$, the electromagnet is either positively charged (+C) or negatively charged (–C) depending on the sign of u_{MN}; when $In1 = In2$, the electromagnet is effectively short-circuited with $u_{MN} \approx 0\ V$ and its magnetic energy is dissipated during the discharging (DC) mode.

TABLE 2. Three modes of full-bridge PWM inverter with electromagnet.

Symbol	$In1$ = HIGH	$In1$ = LOW
$In2$ = HIGH	DC: $u_{MN} \approx 0$ V.	–C: $u_{MN} \approx -U$.
$In2$ = LOW	+C: $u_{MN} \approx +U$.	DC: $u_{MN} \approx 0$ V.

Meanwhile, in Table 3, four quadrants [2] are defined according to u_{MN} and i_{MN}. Generally, the energy flows from the power supply into the electromagnet ($|u_{MN}| < U$) during the forwards charging (FC) mode and flows from the electromagnet into the power supply ($|u_{MN}| > U$) during the backwards charging (BC) mode.

TABLE 3. Four quadrants of full-bridge PWM inverter with electromagnet.

	$u_{MN} \approx -U$	$u_{MN} \approx +U$
$i_{MN} > 0$	(2nd quadrant) –BC: $u_{MN} < -U$.	(1st quadrant) +FC: $u_{MN} < +U$.
$i_{MN} < 0$	(3rd quadrant) –FC: $u_{MN} > -U$.	(4th quadrant) +BC: $u_{MN} > +U$.

In the present work, $In1$ is the PWM signal and $In2$ is obtained by the NOT gate as,

$$In1 = PWM \text{ and } In2 = \overline{PWM}, \tag{2}$$

where the PWM signal can be explicitly expressed as,

$$PWM = \begin{cases} \text{HIGH}, & nT < t < (n+D)\,T \\ \text{LOW}, & (n+D)\,T < t < (n+1)\,T' \end{cases} \tag{3}$$

where T $(= 1/f_{PWM})$ denotes the PWM period, $D \in [0, 1]$ denotes the PWM duty cycle, and n is any arbitrary integer.

B. IDEAL SCENARIO

Assuming the ideal full-bridge PWM inverter, u_{MN} can be expressed by referring to Table 2, (2) and (3) as,

$$u_{MN} = \begin{cases} +U, & nT < t < (n+D)\,T \\ -U, & (n+D)\,T < t < (n+1)\,T \end{cases} \tag{4}$$

Moreover, denote the equilibrium current at $t = nT$ as I_1 and that at $t = (n + D)\,T$ as I_2. Solving (1) together with (4) gives the two equilibrium currents as,

$$\begin{cases} I_1 = \dfrac{U}{R}\left(e^{-T/\tau} + 1 - 2e^{-(1-D)T/\tau}\right) \Big/ \left(e^{-T/\tau} - 1\right) \\ I_2 = \dfrac{U}{R}\left(2e^{-DT/\tau} - e^{-T/\tau} - 1\right) \Big/ \left(e^{-T/\tau} - 1\right), \end{cases} \tag{5}$$

where $\tau = L/R$ denotes the time constant of the electromagnet. Hence, (5) indicates that i_{MN} fluctuates between I_1 and I_2.

Assuming τ to be much larger than T, i.e., $T/\tau \ll 1$, (5) can be approximated as,

$$i_{MN} \approx I_1 \approx I_2 \approx \frac{U}{R}(2D - 1) \in \left[-U/R, U/R\right], \tag{6}$$

which indicates that ideal i_{MN} in the electromagnet is linear with the duty cycle for a high f_{PWM}.

C. NONLINEARITY

Fig. 2 shows the experiment rig for the $i_{MN} - D$ characteristic of the L298N full-bridge PWM inverter. i_{MN} is measured by the ammeter, u_{MN} is measured by the oscilloscope, whereas the PWM signal is generated by the pulse generator.

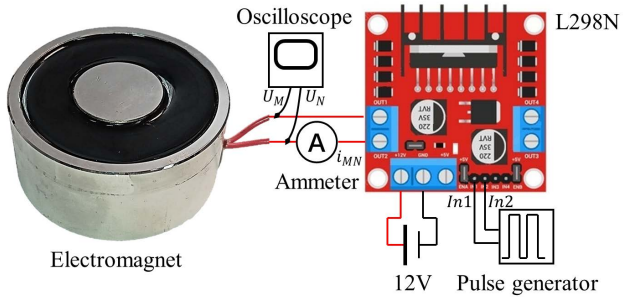

FIGURE 2. Experiment rig for the $i_{MN} - D$ characteristic of L298N full-bridge PWM inverter.

Fig. 3(a) visualizes the variations of i_{MN} w.r.t. D for f_{PWM} = 0.1, 1, 10, 100kHz. It is observed that the characteristic $i_{MN} - D$ curve, e.g., $i_{MN} = f_I(D)$, is an odd function about Point (0.5, 0) as,

$$f_I(1 - D) = -f_I(D). \tag{7}$$

Also, the characteristic $i_{MN} - D$ curve deviates from the ideal scenario in (6), and the deviation increases with the increase of f_{PWM}.

Moreover, define the sensitivity of i_{MN} w.r.t. D as,

$$S = di_{MN}/dD. \tag{8}$$

Fig. 3(b) visualizes the variations of S w.r.t. D. It is observed that S at $D = 0.5$ decreases with the increase of f_{PWM} (as low as 70 mA for 100 kHz), whereas the four sensitivity curves converge to around 1700 mA for $D < 0.3$ and $D > 0.7$. In other words, with the increase of f_{PWM}, the accumulation of the magnetic energy around $D = 0.5$ is weaken.

Furthermore, since F is linear with i_{MN} [14], the large sensitivity change about the zero current (e.g., around 1700/70 ≈ 24.3 times for 100 kHz) will significantly undermine the control stability of the zero-power PEMS system.

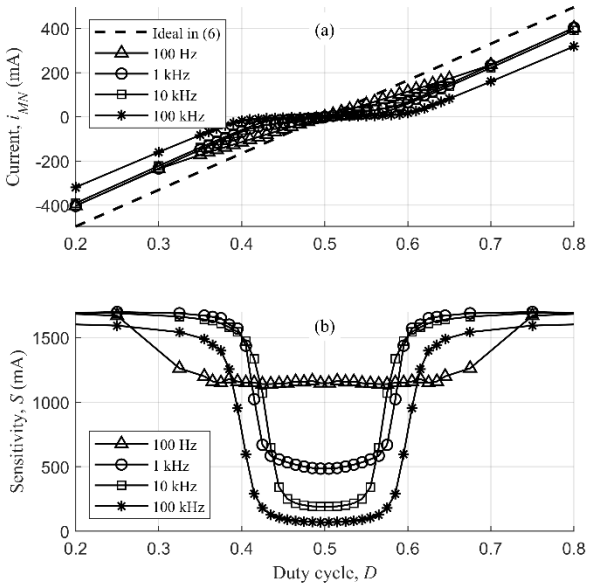

FIGURE 3. Variations of (a) i_{MN} and (b) S w.r.t. D for f_{PWM} = 0.1, 1, 10, 100 kHz.

III. NONLINEAR ANALYSIS

This section analyzes the nonlinear mechanism of the $i_{MN} - D$ characteristic for the electromagnet driven by the L298N full-bridge PWM inverter. Firstly, the voltage dynamics is investigated for two f_{PWM} (one ultra-high and one ultra-low) and $D = 0.5$. Secondly, DC, FC and BC modes are respectively characterized. Thirdly, the critical PWM frequency (f_{cr}) is modelled from the energy perspective. Fourthly, the sensitivity transition is analyzed w.r.t. f_{cr}.

A. VOLTAGE DYNAMICS

1) f_{PWM} = 100 kHz (ULTRA-HIGH)

Fig. 4 visualizes the whole-period variations of $In1$, $In2$, U_M, U_N, and u_{MN} for $f_{PWM} = 100$ kHz and $D = 0.5$ w.r.t. the time (t). It is observed that the dynamic responses of $In1$ and $In2$ are so fast that the step change is completed in less than 0.1 μs, the rising and falling step changes of U_M and U_N are completed in 0.2 μs and 1 μs, respectively. However, by

comparing Figs. 4(a-b), there is a significant delay for around 2 μs between the falling step changes of U_M (or U_N) and $In1$ (or $In2$), which is referred to as the turn-off delay in the datasheet of the L298N full-bridge PWM inverter produced by STMicroelectronics. Therefore, the 2 μs turn-off delay results in the DC mode as defined in Table 2 and highlighted in Fig. 4(c).

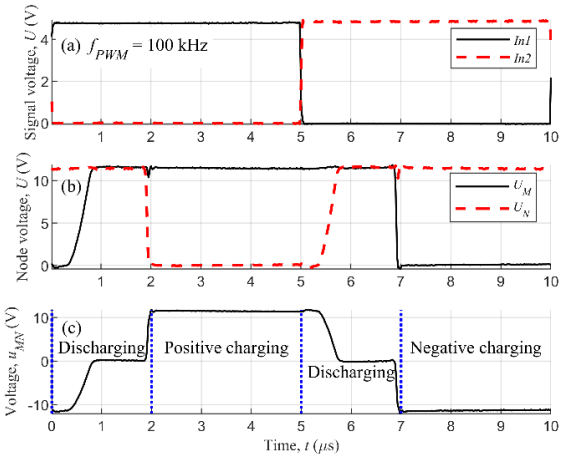

FIGURE 4. Whole-period variations of (a) $In1$ and $In2$, (b) U_M and U_N, and (c) u_{MN} for $f_{PWM} = 100$ kHz and $D = 0.5$ w.r.t. t. The 2 μs turn-off delay due to the L298N full-bridge PWM inverter can be clearly observed for both U_M and U_N in (b) and results in the DC mode in (c). Three modes are highlighted in (c) according to u_{MN}.

2) $f_{PWM} = 100$ Hz (ULTRA-LOW)

Fig. 5 visualizes the whole-period variation of u_{MN} for $f_{PWM} = 100$ Hz and $D = 0.5$ w.r.t. t. Since the 2 μs turn-off delay is negligible compared with the 10 ms PWM period, the variations of $In1$, $In2$, U_M, and U_N are trivial and not shown. As defined in Table 3, the BC and FC modes are separated by the boundaries at $u_{MN} = \pm 12$V in Fig. 5.

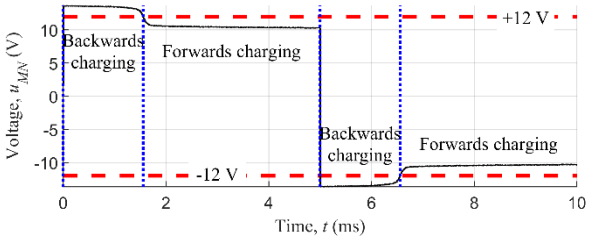

FIGURE 5. Whole-period variation of u_{MN} for $f_{PWM} = 100$ Hz and $D = 0.5$ w.r.t. t. The red dashed lines ($u_{MN} = \pm 12$V) indicate the boundaries between the FC and BC modes.

B. ELECTRONIC CHARACTERISTIC

1) DISCHARGING CHARACTERISTIC

Fig. 6 visualizes the step-change responses of u_{MN} in the initial 3 μs for $f_{PWM} = 5, 10, 20, 50$, and 100 kHz and $D = 0.5$. It is observed that all five curves undergo the 2 μs DC mode. However, the BC mode ($u_{MN} > +12$V) occurs immediately after the DC mode for $f_{PWM} = 5$ and 10 kHz, whereas the FC mode ($u_{MN} < +12$V) occurs for $f_{PWM} = 20$, 50, and 100 kHz.

Technically, the energy-dissipation capability of the DC mode is finite in the 2 μs duration. Therefore, the immediate occurrence of the FC mode indicates that the magnetic energy is entirely dissipated by the DC mode for $f_{PWM} = 20$, 50, and 100 kHz, whereas the magnetic energy exceeds the energy-dissipation capability of the DC mode for $f_{PWM} = 5$ and 10 kHz.

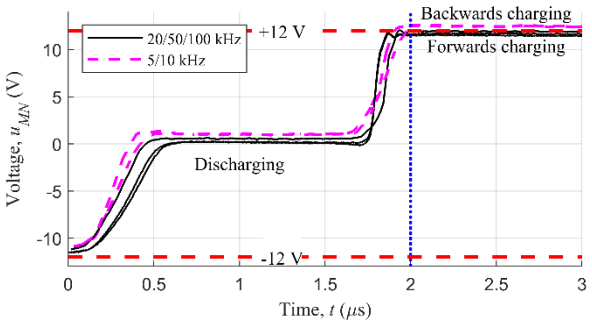

FIGURE 6. Initial-3-μs variations of u_{MN} w.r.t. t for $f_{PWM} = 5$, 10, 20, 50, and 100 kHz and $D = 0.5$. The red dashed lines ($u_{MN} = \pm 12V$) indicate the boundaries between the FC and BC modes.

2) CHARGING CHARACTERISTIC

Fig. 7 visualizes the step-change responses of u_{MN} in the initial 20 ms for $f_{PWM} = 2, 10, 20, 50, 100$, and 200 Hz and $D = 0.5$. The six curves undergo the BC mode before the FC mode. Moreover, it is observed that the curves for $f_{PWM} = 2$, 10, and 20 Hz have a long BC mode for around 5 ms and a long FC mode for around 9 ms, and fluctuate around +10 V afterwards. On the contrary, the curves for $f_{PWM} = 50$, 100, and 200 Hz have shorter BC mode and falls out of the scope before reaching +10 V.

Technically, the charging characteristic is determined by the power supply (e.g., supply voltage and inner resistance) and the electromagnet (e.g., inductance and resistance). Therefore, the saturation at $u_{MN} = \pm 10$V indicates that the electromagnet is entirely charged by the FC mode for $f_{PWM} = 2$, 10, and 20 Hz but is partially charged due to the insufficient duration for $f_{PWM} = 50$, 100, and 200 Hz. Besides, $u_{MN} = \pm 9.5$V can be regarded as the boundary between the DC mode and the two charging modes for the present experimental setup.

C. CRITICAL PWM FREQUENCY

1) EXPERIMENTAL OBSERVATION

Fig. 8 visualizes the contour of u_{MN} w.r.t. $\log_{10}(f_{PWM})$ and the normalized time (t/T) for $D = 0.5$. It is observed that the BC regime expends for $f_{PWM} \leq 100$ Hz, shrinks for $f_{PWM} > 100$ Hz, and vanishes at $f_{PWM} \approx 20$ kHz, whereas the DC regime expends exponentially. Besides, u_{MN} reaches the saturation at ± 10 V only for $f_{PWM} < 10^{1.5}$Hz ≈ 31.6Hz and is increasingly undercharged for $f_{PWM} > 31.6$ Hz.

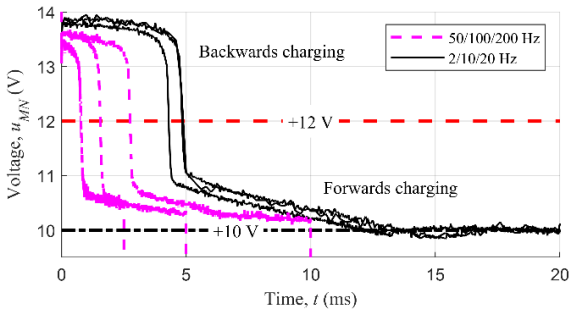

FIGURE 7. Initial-20-ms variations of u_{MN} w.r.t. t for f_{PWM} = 2, 10, 20, 50, 100, and 200 Hz and D= 0.5. Note that the 2 Hz and 10 Hz curves almost overlap with each other. The red dashed lines (u_{MN}= ±12V) indicate the boundaries between the FC and BC modes. The black dash-dot line (u_{MN}= +10V) indicates the saturation of the FC mode.

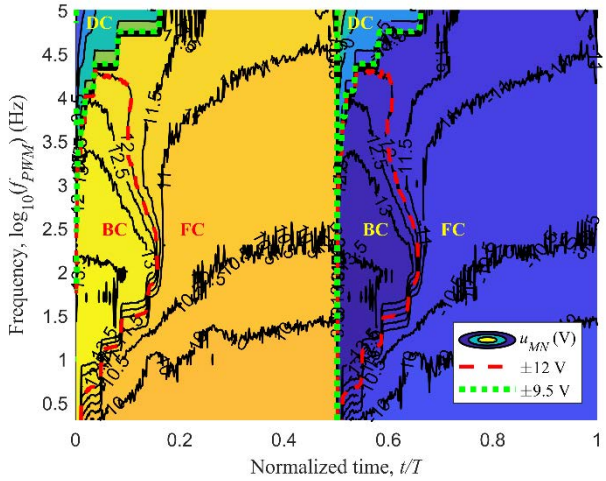

FIGURE 8. Contour of u_{MN} w.r.t. $\log_{10}(f_{PWM})$ and t/T for D = 0.5. The red dashed lines (u_{MN} = ±12V) indicate the boundaries between the FC and BC modes. The green dotted curves (u_{MN} = ±9.5V) indicate the boundaries between the DC mode and the two charging modes.

Moreover, Table 4 lists out the relative portions of the three modes for various f_{PWM} and $D = 0.5$. Note that T_{FC}, T_{BC}, and T_{DC} (= 2 μs) denote durations of FC, BC, and DC modes, respectively.

TABLE 4. Relative portions of three modes for various f_{PWM} and D = 0.5.

f_{PWM} (kHz)	1	2	5	10	20	50	100
T_{BC}/T (%)	11.23	9.33	8.08	6.85	**0.00**	**0.00**	**0.00**
T_{DC}/T (%)	0.40	0.80	2.00	4.00	8.00	20.00	40.00
T_{FC}/T (%)	88.37	89.87	89.92	89.15	92.00	80.00	60.00

2) THEORETICAL ANALYSIS

For $D = 0.5$, the magnetic energy (E) in the electromagnet is charged by the FC mode and dissipated by the DC and BC modes. And, the energy balance equation can be expressed as,

$$E_{FC} = E_{DC} + E_{BC}, \tag{9}$$

where E_{FC}, E_{DC}, and E_{BC} denote the charged energy by the FC mode and the dissipated energies by the DC and BC modes, respectively.

Moreover, assuming $T \ll \tau$, E_{FC}, E_{DC}, and E_{BC} can be linearized and approximated as,

$$E_{FC} = e_{FC}T_{FC}, E_{DC} = e_{DC}T_{DC}, E_{BC} = e_{BC}T_{BC}, \tag{10}$$

where e_{FC}, e_{DC}, and e_{BC} denote the energy-charging rate by the FC mode, and the energy-dissipating rates by the DC and BC modes, respectively.

Assuming $T_{DC} > 0$, substituting (10) into (9) gives,

$$T_{FC}/T_{DC} = (e_{BC}/e_{FC})(T_{BC}/T_{DC}) + e_{DC}/e_{FC}, \tag{11}$$

which is in the first-order form, i.e., $y = ax + b$, where $y = T_{FC}/T_{DC}$, $x = T_{BC}/T_{DC}$, $a = e_{BC}/e_{FC}$, and $b = e_{DC}/e_{FC}$.

By substituting (x, y) associated with f_{PWM} = 1, 2, 5, and 10 kHz in Table 4 into (11), (a, b) can be solved by the least square method as,

$$a = e_{BC}/e_{FC} = 7.46 \text{ and } b = e_{DC}/e_{FC} = 15.33, \tag{12}$$

which indicates that the energy-dissipating rate by the DC mode is around twice as much as that by the BC mode. Therefore, the DC mode gradually replaces the BC mode with the increase of f_{PWM}, which leads to the lower sensitivity as well as the larger energy loss for D = 0.5 as shown in Fig. 3(b).

Furthermore, f_{cr} is defined as the vanishing point of the BC regime (T_{BC} = 0) for D = 0.5 and can be expressed from (11) as,

$$f_{cr} = \frac{1}{T_{FC} + T_{DC}} = \frac{1}{(1 + e_{DC}/e_{FC})} \frac{1}{T_{DC}}, \tag{13}$$

which gives f_{cr}= 15.28 kHz.

Table 5 lists out the estimated relative portions of the three modes by (12) and the associated errors for f_{PWM} = 1, 2, 5, and 10 kHz and D = 0.5. For example, the error (=0.18%) for f_{PWM} = 1 kHz is the difference between T_{BC}/T (=11.23%) and estimated T_{BC}/T (=11.05%).

Therefore, the first-order estimation for the magnetic energy is generally acceptable with low errors.

TABLE 5. Estimated relative portions of three modes and associated errors for various f_{PWM} and D = 0.5.

f_{PWM} (kHz)	1	2	5	10	f_{cr} = 15.28	50
Estimated T_{BC}/T (%)	11.05	10.28	7.96	4.10	0.00	0.00
Estimated T_{DC}/T (%)	0.40	0.80	2.00	4.00	6.13	20.00
Estimated T_{FC}/T (%)	88.55	88.92	90.04	91.90	93.87	80.00
Error (%)	0.18	-0.95	0.12	2.75	-	-

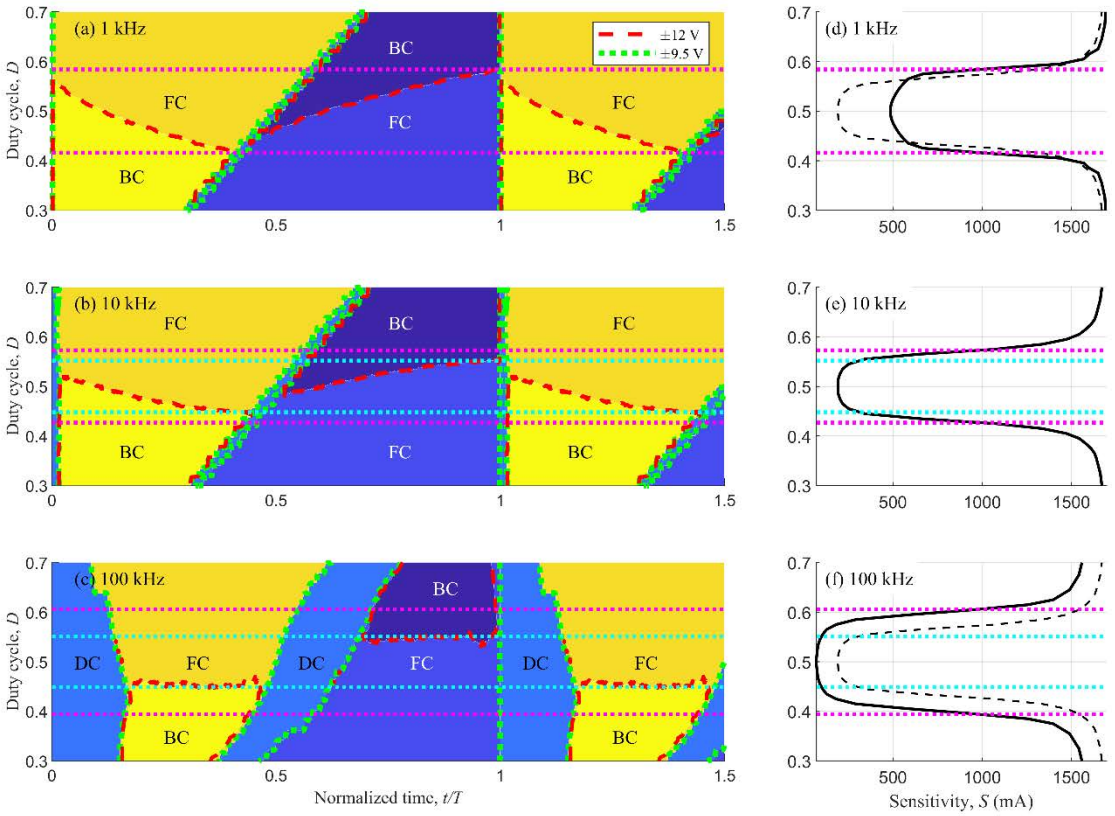

FIGURE 9. (a-c) Phase diagrams of u_{MN} w.r.t. D and t/T, and (d-f) variations of S w.r.t. D for f_{PWM} = 1, 10, and 100 *kHz*. The red dashed lines ($u_{MN} = \pm 12V$) indicate the boundaries between the FC and BC modes. The green dotted curves ($u_{MN} = \pm 9.5V$) indicate the boundaries between the DC mode and the two charging modes. The cyan dotted lines indicate the termination points of the FC regimes, whereas the purple dotted lines indicate the transition points with S = 1000 *mA*. The dashed curve in (d&f) is the benchmark curve with f_{PWM} = 10 kHz.

D. SENSITIVITY TRANSITION

1) EXPERIMENTAL OBSERVATION

Figs. 9(a-c) visualize the phase diagrams of u_{MN} w.r.t. D and t/T for $f_{PWM} = 1,\ 10,$ and 100 kHz. It is observed that the boundaries between the FC and BC regimes are almost continuous for $f_{PWM} = 1$ kHz as a result of the negligible DC regime, whereas the BC regime is heavily squeezed by the DC regime for $f_{PWM} = 100$ kHz. Besides, the cyan dotted lines indicate the termination points of the FC regimes.

Moreover, Figs. 9(d-f) visualize the associated variations of S. The purple dotted lines indicate the transition points with $S = 1000$ mA. It is observed that the three sensitivity curves converge to the high sensitivity outside the purple dotted lines; the three curves stay near the respective minimum values between the cyan dotted lines; meanwhile, the sensitivity transitions take place between the purple and cyan dotted lines.

TABLE 6. Evolution of three modes w.r.t. $D \geq 0.5$ for $f_{PWM} < f_{cr}$.

Stage	DT		$(1-D)T$			Zone
V ($D \approx 1$)	DC	+FC	DC	–BC		High sensitivity
IV	DC	+FC	DC	–BC		Sensitivity transition
III	DC	+FC	DC	–BC	–FC	Low sensitivity
II	DC	+FC	DC	–BC	–FC	
I ($D \approx 0.5$)	DC	+BC +FC	DC	–BC	–FC	

TABLE 7. Evolution of three modes w.r.t. $D \geq 0.5$ for $f_{PWM} > f_{cr}$.

Stage	DT		$(1-D)T$			Zone
V ($D \approx 1$)	DC	+FC	DC	–BC		High sensitivity
IV	DC	+FC	DC	–BC		Sensitivity transition
III	DC	+FC	DC	–BC	–FC	Low sensitivity
II	DC	+FC	DC	–FC		
I ($D \approx 0.5$)	DC	+FC	DC	–FC		

2) THEORETICAL ANALYSIS

Based on Fig. 9, Table 6 and Table 7 outline the evolution of the three modes w.r.t. $D \geq 0.5$ for $f_{PWM} < f_{cr}$ and $f_{PWM} > f_{cr}$, respectively. The red background indicates $i_{MN} > 0$, the blue background indicates $i_{MN} < 0$, and the green background indicates $i_{MN} \approx 0$.

By referring to Table 6 and Table 7, the variations of S can be characterized into three zones from the energy perspective:

- **Low-sensitivity zone**(*Stages I, II, and III, between the cyan dotted lines*): Both +FC and –FC modes co-exist, which indicates that the magnetic energy stored during the FC mode (*both positive and negative*) is completely dissipated by the DC or BC mode. Hence, the low-sensitivity zone is dominated by the energy cancellation between the FC and BC modes for $f_{PWM} < f_{cr}$ and between the FC and DC modes for $f_{PWM} > f_{cr}$. Besides, since the energy-dissipating rate by the DC mode is larger than that by the BC mode in (12), the sensitivity for $D = 0.5$ decreases with the increase of f_{PWM}.
- **Sensitivity-transition zone**(*Stage IV, between the purple and cyan dotted lines*): The 2 μs DC mode has a finite energy-dissipation capability and buffers the sensitivity transition until the capability is entirely consumed, as outlined by the purple and cyan dotted lines. Therefore, the sensitivity transition expends with the increase of f_{PWM}.
- **High-sensitivity zone** (*Stage V, outside the purple dotted lines*): The expending of the FC regime and the shrinking of the BC regime occur simultaneously with the increase of the duty cycle, whereas the current in the electromagnet does not change the direction. Therefore, the magnetic energy accumulates more effectively and the corresponding sensitivity is larger in the high-sensitivity zone than those in the low-sensitivity zone.

IV. CONCLUSION

The present work investigates into the electronic nonlinear of the L298N full-bridge PWM inverter for the zero-power PEMS system. Based on the experimental observation and the theoretical analysis, we can draw the following conclusions:

- In micro level, it is observed that the L298N full-bridge PWM inverter possesses a 2 μs turn-off delay that leads to the passive DC mode; in macro level, such a tiny delay results in the nonlinear $i_{MN} - D$ characteristic.
- With the increase of f_{PWM}, the relative portion of the 2 μs DC mode is significantly amplified and the DC mode replaces the BC mode entirely at $f_{cr} = 15.28$ kHz and $D = 0.5$, which is theoretically modelled from the energy perspective.
- Since the energy-dissipating rate by the DC mode is around twice as much as that by the BC mode, the sensitivity as well as the energy efficiency at $D = 0.5$ decrease with the increase of f_{PWM}.
- The sensitivity transition results from the finite energy-dissipation capability of the 2 μs DC mode and expends with the increase of f_{PWM}.
- A full-bridge PWM inverter with a lower turn-off delay will result in a higher f_{cr} and be more preferable, such as CM75TF-12H (IGBT produced by MITSUBISHI, with a 0.2 μs turn-off delay)[8].
- Though higher f_{PWM} can enhance the dynamic performance of the high-speed PEMS transportation system [20], a slightly smaller f_{PWM} than f_{cr} is more preferable due to the higher energy efficiency and the gentler sensitivity transition, whereas the suitable compensation measures are necessary to take care of the nonlinear $i_{MN} - D$ characteristic, e.g., the bias current [3], [17] and the close-loop current control [2], [4], [7], [8], [10], [11].

CONFLICTS OF INTEREST

The authors declare no conflict of interest.

REFERENCES

[1] H.-W. Lee, K.-C. Kim, and J. Lee, "Review of Maglev train technologies," *IEEE Trans. Magn.*, vol. 42, no. 7, pp. 1917–1925, Jul. 2006, doi: 10.1109/Tmag.2006.875842.
[2] T. Schuhmann, W. Hofmann, and R. Werner, "Improving operational performance of active magnetic bearings using Kalman filter and state feedback control," *IEEE Trans. Ind. Electron.*, vol. 59, no. 2, pp. 821–829, Feb. 2012, doi: 10.1109/TIE.2011.2161056.
[3] G.-P. Ren, Z. Chen, H.-T. Zhang, Y. Wu, H. Meng, D. Wu, and H. Ding, "Design of interval type-2 fuzzy controllers for active magnetic bearing systems," *IEEE/ASME Trans. Mechatronics*, vol. 25, no. 5, pp. 2449–2459, Oct. 2020, doi: 10.1109/TMECH.2020.2978018.
[4] S.-L. Chen, S.-Y. Lin, and C.-S. Toh, "Adaptive unbalance compensation for a three-pole active magnetic bearing system," *IEEE Trans. Ind. Electron.*, vol. 67, no. 3, pp. 2097–2106, Mar. 2020, doi: 10.1109/TIE.2019.2903747.
[5] Z. G. Liu, Z. Q. Long, and X. L. Li, *Maglev Trains: Key Underlying Technologies* (Tracts in Mechanical Engineering), 1st ed. Berlin, Germany: Springer, 2015.
[6] Z. Zhang, C. Shang, L. She, W. Chang, and L. Zhang, "Structural optimal design of a permanent-electro magnetic suspension magnet for middle-low-speed maglev trains," *IET Electr. Syst. Transp.*, vol. 1, no. 2, pp. 61–68, Jun. 2011, doi: 10.1049/iet-est.2010.0018.
[7] H. Zhu and T. Liu, "Rotor displacement self-sensing modeling of six-pole radial hybrid magnetic bearing using improved particle swarm optimization support vector machine," *IEEE Trans. Power Electron.*, vol. 35, no. 11, pp. 12296–12306, Nov. 2020, doi: 10.1109/TPEL.2020.2982746.
[8] R.-J. Wai, J.-D. Lee, and K.-L. Chuang, "Real-time PID control strategy for maglev transportation system via particle swarm optimization," *IEEE Trans. Ind. Electron.*, vol. 58, no. 2, pp. 629–646, Feb. 2011, doi: 10.1109/Tie.2010.2046004.
[9] W. Feng, F. C. Lee, and P. Mattavelli, "Simplified optimal trajectory control (SOTC) for LLC resonant converters," *IEEE Trans. Power Electron.*, vol. 28, no. 1, pp. 457–466, May 2013, doi: 10.1109/TPEL.2012.2200110.
[10] B. C. Yalcin and K. Erkan, "3-DoF zero power micro vibration isolation via linear matrix inequalities based on H_∞ and H_2 control approaches," *Mech. Syst. Signal Process.*, vol. 153, no. 2021, p. 107506, Dec. 2021, doi: 10.1016/j.ymssp.2020.107506.
[11] X. Sun, Z. Jin, L. Chen, and Z. Yang, "Disturbance rejection based on iterative learning control with extended state observer for a four-degree-of-freedom hybrid magnetic bearing system," *Mech. Syst. Signal Process.*, vol. 153, May 2021, Art. no. 107465, doi: 10.1016/j.ymssp.2020.107465.
[12] M. Morishita and T. Azukizawa, "Zero power control of electromagnetic levitation system," *Electr. Eng. Jpn.*, vol. 108, no. 3, pp. 111–120, May 1988, doi: 10.1002/eej.4391080313.
[13] T. Mizuno, M. Takasaki, D. Kishita, and K. Hirakawa, "Vibration isolation system combining zero-power magnetic suspension with springs," *Control Eng. Pract.*, vol. 15, no. 2, pp. 187–196, Feb. 2007, doi: 10.1016/j.conengprac.2006.06.001.
[14] Z. Zhang, T. Gao, Y. Qin, J. Yang, and F. Zhou, "Numerical study for zero-power maglev system inspired by undergraduate project kits," *IEEE Access*, vol. 8, pp. 90316–90323, 2020, doi: 10.1109/access.2020.2994128.
[15] Y.-K. Tzeng and T. C. Wang, "Dynamic analysis of the Maglev system using controlled-PM electromagnets and robust zero-power-control strategy," *IEEE Trans. Magn.*, vol. 31, no. 6, pp. 4211–4213, Nov. 1995, doi: 10.1109/20.489929.
[16] S.-Y. Cho, W.-H. Kim, I.-S. Jang, D.-W. Kang, and J. Lee, "Robust zero power levitation control of quadruple hybrid EMS system," *J. Electr. Eng. Technol.*, vol. 8, no. 6, pp. 1451–1456, Nov. 2013, doi: 10.5370/Jeet.2013.8.6.1451.

[17] H. Sheh Zad, T. I. Khan, and I. Lazoglu, "Design and adaptive sliding-mode control of hybrid magnetic bearings," *IEEE Trans. Ind. Electron.*, vol. 65, no. 3, pp. 2537–2547, Mar. 2018, doi: 10.1109/tie.2017.2739682.
[18] S. H. Lee, H. K. Sung, J. T. Lim, and Z. Bien, "Self-tuning control of electromagnetic levitation systems," *Control Eng. Pract.*, vol. 8, no. 7, pp. 749–756, Sep. 2000, doi: 10.1016/S0967-0661(00)00005-8.
[19] S. Banerjee, M. K. Sarkar, P. K. Biswas, R. Bhaduri, and P. Sarkar, "A review note on different components of simple electromagnetic levitation systems," *IETE Tech. Rev.*, vol. 28, no. 3, pp. 256–264, May 2011, doi: 10.4103/0256-4602.81241.
[20] Z. Wang, Z. Long, and X. Li, "Track irregularity disturbance rejection for maglev train based on online optimization of PnP control architecture," *IEEE Access*, vol. 7, pp. 12610–12619, 2019, doi: 10.1109/ACCESS.2019.2891964.

LEI CHEN received the bachelor's degree from Nanchang Hangkong University, in 2010, and the master's degree from the Guangdong University of Technology, in 2013. He is currently a Lecturer with the Jiangxi College of Applied Technology. His research interest includes mechanics, electronics, and automatic control.

JINMEI GUO received the bachelor's and master's degrees from the Jiangxi University of Science and Technology, in 2012 and 2015, respectively. She is currently a Lecturer with the Jiangxi College of Applied Technology. Her research interests include electric automation and artificial intelligence.

BIN ZHU received the bachelor's and master's degrees from Wuyi University, in 2005 and 2008, respectively, and the doctor's degree from the South China University of Technology, in 2019. He is currently a Vice Professor with the Jiangxi College of Applied Technology. His research interests include image processing and deep learning.

ZEYI ZHANG received the bachelor's and Ph.D. degrees from The University of Hong Kong, in 2014 and 2018, respectively. He is currently a Vice Professor with the School of Electrical Engineering and Automation, Jiangxi University of Science and Technology. His research interests include permanent maglev and automatic control.